Dynamical cluster approximation employing the fluctuation exchange approximation as a cluster solver

K. Aryanpour,[1] M. H. Hettler,[2] and M. Jarrell[1]

[1]*University of Cincinnati, Cincinnati Ohio 45221*
[2]*Forschungszentrum Karlsruhe, Institut für Nanotechnologie, Karlsruhe, Germany*

We employ the dynamical cluster approximation (DCA) in conjunction with the fluctuation exchange approximation (FLEX) to study the Hubbard model. The DCA is a technique to systematically restore the momentum conservation at the internal vertices of Feynman diagrams relinquished in the dynamical mean field approximation. The FLEX is a perturbative diagrammatic approach in which classes of Feynman diagrams are summed over analytically using geometric series. The FLEX is used as a tool to investigate the complementarity of the DCA and the finite size lattice technique with periodic boundary conditions by comparing their results for the Hubbard model. We also study the microscopic theory underlying the DCA in terms of compact (skeletal) and noncompact diagrammatic contributions to the thermodynamic potential independent of a specific model. The significant advantages of the DCA implementation in momentum space suggests the development of the same formalism for the frequency space. However, we show that such a formalism for the Matsubara frequencies at finite temperatures leads to acausal results and is not viable. However, a real frequency approach is shown to be feasible.

I. INTRODUCTION

Nonlocal correlations play an important role in the physics of strongly correlated electron systems such as high-T_c superconductors, heavy fermion metals, etc. The dynamical mean field approximation (DMFA),[1,2] in which all the nonlocal correlations are ignored, can capture some of the major features of strongly correlated systems. Nevertheless, the nonlocal correlations become crucial in the physics of phases with nonlocal order parameters such as d-wave superconductivity. Even phases with local order parameters such as commensurate magnetism can be significantly affected by the nonlocal correlations (e.g., spin waves) ignored in the DMFA.

The early attempts to extend the DMFA by including nonlocal correlations resulted in the violation of causality which is a requirement for positive definiteness of the spectral weight and the density of states (DOS).[3] The dynamical cluster approximation (DCA) is a fully causal technique used to systematically add nonlocal corrections to the DMFA by mapping the lattice onto a self-consistently embedded cluster problem. The mapping from the lattice to the cluster is accompanied by coarse graining the lattice problem in its reciprocal space. Thus far, the DCA has been combined with the quantum Monte Carlo (QMC) approximation,[4,5] the noncrossing approximation (NCA),[6] and the fluctuation exchange approximation (FLEX) (Refs. 11 and 12) to solve the corresponding cluster problems.

The FLEX is a perturbative diagrammatic approach in which classes of Feynman diagrams are summed to all orders using geometric series.[7,8] Others[9,10] have employed the FLEX for finite size lattices with periodic boundary conditions. Due to the absence of contributions from some relevant diagrams, the FLEX is not capable of addressing the Hubbard model physics in the strong regime precisely. However, the main objective of this work is to make a comparison between the DCA-FLEX combination results and previous finite size lattice FLEX calculations. It is hoped that this study will lead to a better understanding of the DCA.

We earlier[11] suggested a prescription to correctly implement the DCA technique in the thermodynamic potential. This prescription will be discussed from a different point of view using a more general argument. Based upon the Green function's exponential falloff as a function of distance, we conclude that compact diagrams (two-particle irreducible in the thermodynamic potential) are better approximated using the DCA than noncompact (two-particle reducible) ones. Hence the DCA is applied to the compact diagrams only, and noncompact ones are calculated explicitly using dressed non coarse grained Green functions.

In this work we also consider the extension of the DCA to frequency space. The many-body theory at finite temperatures is conventionally derived in terms of discrete imaginary Matsubara frequencies. We illustrate that even for a self-consistent algorithm like the FLEX, coarse graining the imaginary frequency propagators results in causality violations and can not be implemented. However, a real frequency formalism is shown to be causal and applicable not only to the FLEX, but also to other cluster solving methods such as the NCA.

This paper is structured as follows. In the next three sections, we briefly review the DCA and its application to the Hubbard model, the FLEX, and then we describe how the FLEX and the DCA may be merged into a single algorithm. In the next three sections, we use the FLEX-DCA, in comparison to the FLEX for finite sized systems, to explore the properties of the DCA. The last two sections, are devoted to a microscopic derivation of the DCA, and to an extension of the DCA to frequency space.
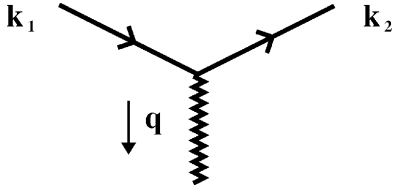
FIG. 1. A typical vertex in a Feynman diagram with solid lines as one-particle Green functions and the wiggly line as an interaction.

II. DYNAMICAL CLUSTER APPROXIMATION (DCA)

Both the DCA and DMFA may be derived by exploring the momentum conservation in the diagrammatics. As depicted in Fig. 1, momentum conservation at each vertex is described by the Laue function:

$$\Delta = \sum_{\mathbf{x}} e^{i\mathbf{x}\cdot(\mathbf{k}_1 - \mathbf{q} - \mathbf{k}_2)} = N\delta_{\mathbf{k}_1, \mathbf{q}+\mathbf{k}_2}, \tag{1}$$

In the DMFA, momentum conservation at the internal vertices of irreducible Feynman diagrams is completely relinquished. That is, the DMFA simply sets $\Delta=1$.[13] Hence we may sum freely over all the internal momenta entering and leaving each vertex. Only local contributions survive the sum. Thus this is equivalent to mapping the lattice problem onto a self-consistently embedded impurity problem. The DMFA becomes exact at infinite dimensions.[14]

The DCA is an approach to systematically restore the momentum conservation relinquished in the DMFA. In the DCA, the first Brillouin zone in the reciprocal space is divided into N_c equal cells of linear size Δk labeled by $\mathbf{K}$ in their centers, and the momenta within each cell are labeled by $\tilde{\mathbf{k}}$. Then $\mathbf{k}=\mathbf{K}+\tilde{\mathbf{k}}$ (cf. Fig. 2). To visualize this scheme in the real lattice, one could consider tiling the lattice of N sites by N/N_c clusters each composed of $N_c=L^D$ sites where L is the linear size of the subcell and D is dimensionality (cf. Fig. 2 for $L=2$). We will use this picture in Sec. VIII while discussing the microscopic theory of the DCA. We label the origin of the clusters by $\tilde{\mathbf{x}}$ and the N_c intercluster sites by $\mathbf{X}$. So for each site in the original lattice $\mathbf{x}=\mathbf{X}+\tilde{\mathbf{x}}$. Care must be taken when choosing the cluster geometries in order to preserve the lattice point group symmetry and also satisfy some other criteria for cubic or square lattices.[15]
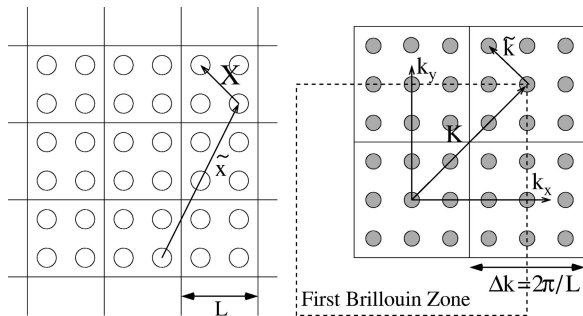

FIG. 2. The real lattice clusters (right) and (left) the first Brillouin zone divided into subcells.

In the DCA, we first make the following separation in Eq. (1):

$$\Delta = \sum_{\mathbf{x}} e^{i(\tilde{\mathbf{x}}+\mathbf{X})\cdot(\mathbf{K}_1 - \mathbf{Q} - \mathbf{K}_2 + \tilde{\mathbf{k}}_1 - \tilde{\mathbf{q}} - \tilde{\mathbf{k}}_2)}. \tag{2}$$

The products $\mathbf{K}_1\cdot\tilde{\mathbf{x}}, \mathbf{Q}\cdot\tilde{\mathbf{x}}$ and $\mathbf{K}_2\cdot\tilde{\mathbf{x}}=2n\pi$, where n is an integer. Therefore, their associated phases may be neglected and Eq. (1) splits into two parts:

$$\Delta = \frac{N}{N_c}\delta_{\tilde{\mathbf{k}}_1, \tilde{\mathbf{q}}+\tilde{\mathbf{k}}_2} N_c \delta_{\mathbf{K}_1, \mathbf{Q}+\mathbf{K}_2}. \tag{3}$$

The DCA also ignores the phases $e^{-i\tilde{\mathbf{k}}\cdot\tilde{\mathbf{x}}}$ due to the position of the cluster in the original lattice and (far less important) $e^{-i\tilde{\mathbf{k}}\cdot\mathbf{X}}$ corresponding to the position within the cluster. As a result, it approximates $N/N_c \delta_{\tilde{\mathbf{k}}_1, \tilde{\mathbf{q}}+\tilde{\mathbf{k}}_2} \cong 1$, so that

$$\Delta_{DCA} = N_c \delta_{\mathbf{K}_1, \mathbf{Q}+\mathbf{K}_2}, \tag{4}$$

which indicates that the momentum is conserved modulo Δk for transfers between the cells.

The approximation made through the substitution $\Delta \rightarrow \Delta_{DCA}$ corresponds to replacing all internal legs in the compact (skeletal) diagrams by the coarse grained Green function $\bar{G}$ and interaction potential $\bar{V}$ defined by

$$\bar{G}(\mathbf{K}, \omega_n) = \frac{N_c}{N}\sum_{\tilde{\mathbf{k}}} G(\mathbf{K}+\tilde{\mathbf{k}}, \omega_n), \tag{5}$$

$$\bar{V}(\mathbf{Q}) = \frac{N_c}{N}\sum_{\tilde{\mathbf{q}}} V(\mathbf{Q}+\tilde{\mathbf{q}}). \tag{6}$$

In Sec. VIII, we will define the compact and noncompact diagrams and elaborately discuss why only the compact ones undergo the coarse graining approximation.

Replacing Δ by Δ_{DCA} tremendously reduces the complexity of the problem because instead of having to perform sums over all N states in the entire first Brillouin zone, we have sums over only a set of N_c states where $N_c \ll N$.

III. HUBBARD MODEL

We will apply the DCA to study the Hubbard model Hamiltonian incorporating interactions between the electrons on a lattice. It includes a tight-binding part due to the hopping of electrons among the sites and an interaction between the electrons. The general Hamiltonian reads

$$H = H_0 + H_I, \tag{7}$$

where

$$H_0 = -t\sum_{\sigma}\sum_{\langle ij\rangle} c_{i\sigma}^\dagger c_{j\sigma} \tag{8}$$

and

$$H_I = \frac{1}{2}\sum_{jl,\sigma\sigma'} n_{j\sigma}n_{l\sigma'} V(R_j - R_l)$$

$$V(R) \approx \frac{e^2}{R}. \qquad (9)$$

Factors t and $V(R)$ correspond to electron hoppings and Coulomb interactions, respectively. Later in the paper, we will study the simplest Hubbard interaction which is fully local and only between electrons sitting at the same site having opposite spin directions. The interaction strength is a constant called U. Hence, for the local model, Eq. (9) simplifies to

$$H_I = U \sum_i n_{i\uparrow} n_{i\downarrow}. \qquad (10)$$

In terms of the vertex properties addressed in Sec. II, since the interaction is local and therefore independent of $\mathbf{q}$, we may sum freely over the $\mathbf{q}$ momentum for a pair of Laue functions in Eq. (1) sharing a common interaction wiggly line as depicted in Fig. 1. As a result, the corresponding Laue function will become

$$\Delta = \frac{1}{N} \sum_{\mathbf{q}} \sum_{\mathbf{x}} e^{i\mathbf{x} \cdot (\mathbf{k}_1 - \mathbf{q} - \mathbf{k}_2)} \sum_{\mathbf{y}} e^{i\mathbf{y} \cdot (\mathbf{k}_3 + \mathbf{q} - \mathbf{k}_4)}$$

$$= N \sum_{\mathbf{q}} \delta_{\mathbf{k}_1, \mathbf{q} + \mathbf{k}_2} \delta_{\mathbf{k}_3 + \mathbf{q}, \mathbf{k}_4} = N \delta_{\mathbf{k}_1 + \mathbf{k}_3, \mathbf{k}_2 + \mathbf{k}_4}, \qquad (11)$$

and analogously for the DCA, by summing freely over $\mathbf{Q}$,

$$\Delta_{DCA} = N_c \, \delta_{\mathbf{K}_1 + \mathbf{K}_3, \mathbf{K}_2 + \mathbf{K}_4}. \qquad (12)$$

IV. FLUCTUATION EXCHANGE APPROXIMATION (FLEX)

In the Feynman diagrammatics of the Hubbard model with a local interaction, all the interactions (wiggly lines in Fig. 3) contribute a c number U from Eq. (10). The electronic Green functions (solid lines) which interact with one another should have opposite spins. Considering these restrictions, had we been able to include all the possible diagrams in our expansion we would have solved the problem exactly. However, in practice this is not feasible.

The FLEX was introduced as an approximate technique to simplify this diagrammatic sum,[7,8] while retaining a conserving approximation. In the FLEX, the interaction part of the Hubbard model Hamiltonian is treated perturbatively by selecting a certain class of all the possible diagrams which may be summed as a geometric series. Following Baym,[16] we define the generating functional $\Phi[G(k, \omega_n)]$ as the collection of all the selected families of diagrams illustrated in Fig. 3. Therefore, $\Phi[G(k, \omega_n)]$ for the FLEX can be written

$$\Phi = \Phi_{ph}^{df} + \Phi_{ph}^{sf} + \Phi_{pp}, \qquad (13)$$

$$\Phi_{ph}^{df} = -\frac{1}{2} \text{Tr}[\chi_{ph}]^2 + \frac{1}{2} \text{Tr}\left[\ln(1 + \chi_{ph}) - \chi_{ph} + \frac{1}{2} \chi_{ph}^2 \right], \qquad (14)$$

$$\Phi_{ph}^{sf} = \frac{3}{2} \text{Tr}\left[\ln(1 - \chi_{ph}) + \chi_{ph} + \frac{1}{2} \chi_{ph}^2 \right], \qquad (15)$$
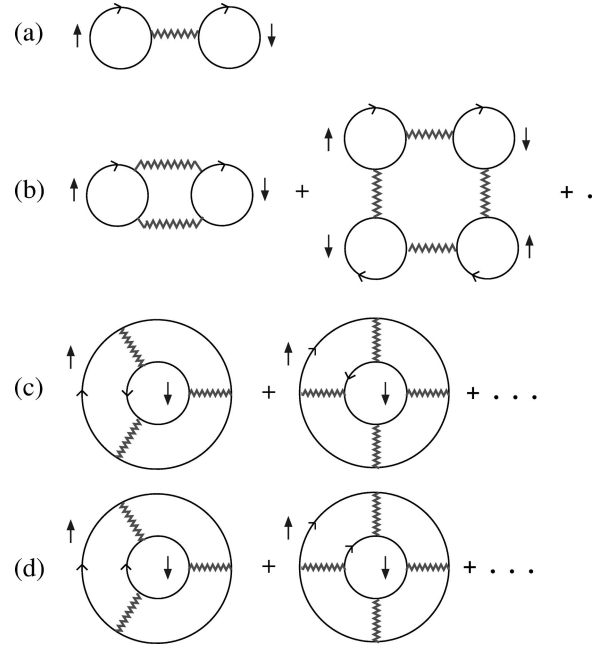

FIG. 3. (a) Lowest order diagram (Hartree term), (b) longitudinal spin and density fluctuation Φ diagrams with an even number of bubbles (Φ_{ph}^{df}), (c) transverse spin fluctuations (Φ_{ph}^{sf}), and (d) particle-particle fluctuations (Φ_{pp}).

$$\Phi_{pp} = \text{Tr}\left[\ln(1 + \chi_{pp}) - \chi_{pp} + \frac{1}{2} \chi_{pp}^2 \right], \qquad (16)$$

where $\text{Tr} = (T/N) \Sigma_k \Sigma_n$ with T the temperature and N the number of lattice sites. The particle-hole and particle-particle susceptibility bubbles are

$$\chi_{pp}(q, \omega_n) = U(T/N) \sum_k \sum_m G(k + q, \omega_n + \omega_m)$$
$$\times G(-k, -\omega_m), \qquad (17)$$

$$\chi_{ph}(q, \omega_n) = -U(T/N) \sum_k \sum_m G(k + q, \omega_n + \omega_m) G(k, \omega_m), \qquad (18)$$

The self-energy and the Green function are defined by

$$\Sigma(k, \omega_n) = \frac{1}{2} \frac{\delta \Phi[G]}{\delta G(k, \omega_n)}, \qquad (19)$$

$$G(k, \omega_n) = [G^{(0)-1}(k, \omega_n) - \Sigma(k, \omega_n)]^{-1}, \qquad (20)$$

where $G^{(0)}$ is the noninteracting one-particle Green function defined by

$$G^{(0)}(\mathbf{k}, \omega_n) = \frac{1}{\omega_n - \epsilon_{\mathbf{k}} + \mu}, \qquad (21)$$

with $\epsilon_{\mathbf{k}}$ the noninteracting Hubbard model dispersion and μ the chemical potential.

Calculating the self-energy for Eq. (13), using Eq. (19), we get

$$\Sigma(k,\omega_n) = U(T/N) \sum_q \sum_m [V^{(ph)}(q,\omega_m)G(k-q,\omega_n-\omega_m)$$

$$- V^{(pp)}(q,\omega_m)G(-k+q,-\omega_n+\omega_m)], \qquad (22)$$

in which

$$V^{(ph)}(q,\omega_m) = \chi_{ph}(q,\omega_m) + \frac{1}{2}\chi_{ph}(q,\omega_m)$$

$$\times \left[\frac{1}{1+\chi_{ph}(q,\omega_m)} - 1\right] + \frac{3}{2}\chi_{ph}(q,\omega_m)$$

$$\times \left[\frac{1}{1-\chi_{ph}(q,\omega_m)} - 1\right], \qquad (23)$$

$$V^{(pp)}(q,\omega_m) = \chi_{pp}(q,\omega_m)\left[\frac{1}{1+\chi_{pp}(q,\omega_m)} - 1\right]. \quad (24)$$

Equations (23) and (24) for the potential functions $V^{(ph)}$ and $V^{(pp)}$ are geometric series for χ_{ph} and χ_{pp} similar to the *random phase approximation* results. The Hartree term contribution to the self-energy has not explicitly appeared in Eq. (22), as it is constant and can be always embedded in the chemical potential in Eq. (21).

The difference $\Delta\Omega(T,\mu)$ between interacting and noninteracting thermodynamic potential functionals is also expressible in terms of the Green functions, self-energy, and $\Phi[G]$:

$$\Delta\Omega(T,\mu) = \Omega - \Omega_0 = -2\text{Tr}[\Sigma G - \ln(G/G_0)] + \Phi[G]. \qquad (25)$$

In the FLEX, since we include only a limited set of all the diagrammatic contributions, we do not anticipate to precisely address the Hubbard model physics. However, there are a number of significant physical features such as antiferromagnetic order at half filling and low temperatures that this approximation is able to capture. Moreover, by using the FLEX together with both the DCA and finite sized systems with periodic boundary conditions, we can study the differences between these approaches. For example, as we will shortly illustrate, the complementarity of the DCA and finite size lattice techniques is manifest in the FLEX. The FLEX can also be invoked as a good test for the microscopic theory of the DCA and the coarse graining effects in the compact and non-compact diagrams for Eq. (25).

V. COMBINATION OF THE FLEX AND DCA (ALGORITHM)

In the combination of the FLEX and DCA, our goal is to calculate the self-energy in Eq. (19) whereby we construct the dressed Green function for the lattice as a building block for all the relevant physical quantities. We start out with the bare (noninteracting) Green function $G^{(0)}(\mathbf{k},z)$ defined in Eq. (21) with z the Matsubara frequency (complex). We coarse grain G as directed in Eq. (5), and calculate the self-energy using Eq. (19). This is used to recompute the dressed Green function
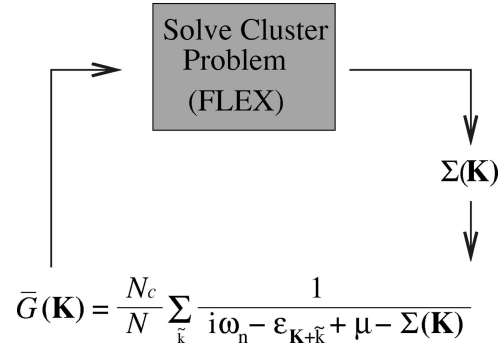

$$\bar{G}(\mathbf{K}) = \frac{N_c}{N} \sum_{\tilde{k}} \frac{1}{i\omega_n - \epsilon_{\mathbf{K}+\tilde{k}} + \mu - \Sigma(\mathbf{K})}$$

FIG. 4. The FLEX-DCA numerical algorithm. The dressed G is solved self-consistently with Σ. The iteration process stops whenever convergence is achieved.

$$G(\mathbf{k},z) = \frac{1}{z - \epsilon_{\mathbf{k}} + \mu - \Sigma_{DCA}(\mathbf{K},z)}. \qquad (26)$$

where the index DCA in $\Sigma_{DCA}(\mathbf{K},z)$ indicates that we have used coarse grained $\bar{G}$ for the construction of self-energy. The new G is coarse grained and used to calculate a new estimate of $\Sigma_{DCA}(\mathbf{K},z)$. We repeat this process iteratively until convergence at a desired tolerance is obtained. The final self-energy is used to construct the dressed Green function in Eq. (26), required to compute the physical quantities such as spectral function, the density of states, etc. The algorithm of this calculation is demonstrated in Fig. 4.

VI. COMPLEMENTARITY OF THE DCA TO THE FINITE SIZE LATTICE APPROXIMATION WITH PERIODIC BOUNDARY CONDITIONS

In the half-filled Hubbard model, the antiferromagnetic correlation length ξ increases with decreasing temperature and diverges at the phase transition. In a finite size lattice with periodic boundary conditions, as the temperature drops, once the correlation length reaches the size of the lattice, the system is fully frozen and there is a gap to excitations [cf. Fig 5(a)]. In contrast, in the DCA, the correlations are confined within clusters of size $N_c \ll N$ (the size of the entire lattice) and they never reach the size of the lattice. As we lower the temperature, the correlation length approaches the size of the cluster, but since the lattice remains in the ther-
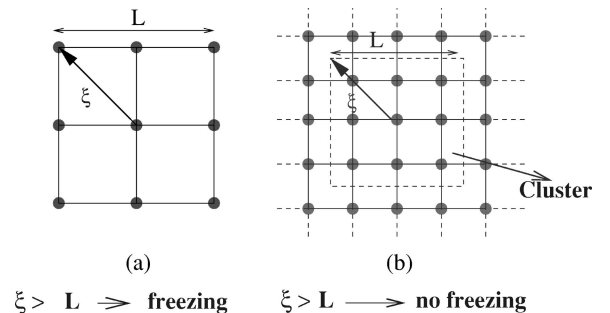

FIG. 5. (a) The finite size lattice with periodic boundary conditions, size L and correlation length ξ and (b) the lattice with clusters of size L and the correlation length ξ.
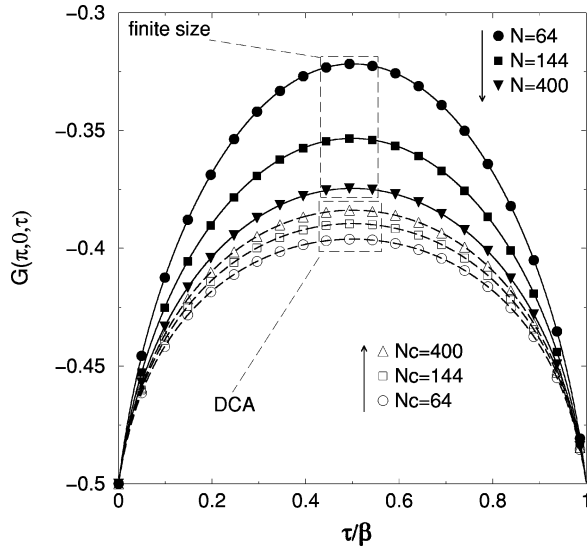
FIG. 6. The Green function $G(k=(0,\pi),\tau)$ at $T=0.10$ and $U/t=1.57$ vs imaginary time τ/β ($\beta=1/T$). Finite size results (filled symbols) and DCA results (open symbols) are displayed for lattice sizes of $N=8\times8$, 12×12, and 20×20. The curves show the complementary approach of the two methods to the thermodynamic limit.
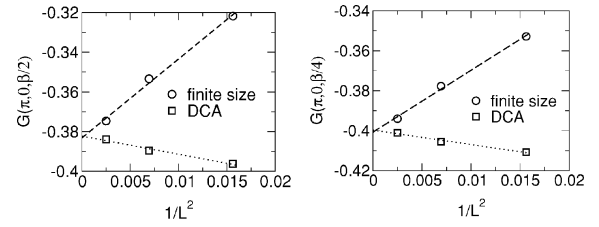

FIG. 7. The Green function $G(k=(0,\pi),\tau)$ at $\tau=\beta/2$ (left) and $\tau=\beta/4$ (right) vs $1/L^2$ for the DCA and finite size results in Fig. 6. The linear extrapolations meet at a point representing the thermodynamic limit of the Green function of the Hubbard model evaluated within the FLEX.

VII. FINITE SIZE VERSUS THE DCA FLEX RESULTS FOR THE TWO-DIMENSIONAL HUBBARD MODEL AT HALF-FILLING

The Hubbard model at half filling undergoes a phase transition to anti-ferromagnetic order at low temperatures. According to the Mermin-Wagner-Hohenberg theorem, for dimension $D=2$ the critical temperature is zero. However, as we continue to lower the temperature, close enough to zero, a pseudogap will appear in the density of states as a precursor to the anti-ferromagnetic phase (which has a full gap as its signature). An approach towards non-Fermi-liquid behavior is also visible in both the real and imaginary parts of the retarded self-energy.[9]

In Figs. 8 and 9, the densities of states for lattices with finite sizes of 32×32 and 64×64 and periodic boundary conditions and coarse graining cluster sizes of 16×16 and 32×32 are plotted. We analytically continue the Green function in order to calculate the spectral function $A(k,\omega)$ and the DOS using the Padé approximation.[18] In this approximation, we generate a continued fraction interpolating all the data points and use it as an analytic function of the Matsubara frequencies ω_n. The analytic continuation is accomplished by substituting ω_n with $\omega+i\eta$, where η is a small positive shift. However, the errors inherent in the numerical Fourier transform (FFT) and also the sharp high-frequency behavior of the Green function, FLEX potentials, and the self-energy limit the accuracy of the Padé approximation. The high-frequency behavior is improved by implementing a more authentic cutoff scheme introduced by Deisz et al.[19] in which the high-frequency tails of these quantities are Fourier transformed analytically prior to any numerical FFT and added back to the FFT outputs afterwards. In addition to this high-frequency cutoff improvement, we also check for the analyticity of the Padé results in the upper-half frequency plane as a requirement for retarded physical quantities. This task is carried out by converting the continued fraction in the Padé approximation into a ratio of two polynomials. The complex roots of these two polynomials are obtained via the Jenkins-Traub root finder routine.[20] Those orders of the Padé approximation for which there exist poles in the upper-half plane are omitted unless these poles are canceled by the roots of the numerator. The acceptable Padé results correspond to the highest order with no uncompensated poles in the upper-half plane.

modynamic limit, it never freezes [cf. Fig 5(b)]. By increasing the size of clusters in the DCA, we take longer ranged correlations into account so the gap will become more pronounced. Consequently, correlation induced gaps are generally overestimated in the finite size lattice, while in the DCA they are underestimated.

This complementary behavior may be seen in $G(k,\tau)$, with $k=(0,\pi)$ computed using finite size lattices with periodic boundary conditions and the DCA. As illustrated in Fig. 6, by increasing the size of the finite size lattice and the DCA cluster, the Green functions converge from opposite directions. In the finite size lattice, the Green function (e.g., at $\tau=\beta/2$) decreases with the increase of size which is consistent with overestimating the gap, while in the DCA the Green function increases as the cluster size grows, consistent with underestimating the gap. It is also observed that the convergence in the DCA is much faster, meaning that the result of the DCA is closer to the true curve at a given cluster size. Both finite size lattices with periodic boundary conditions and the DCA converge with corrections of $\mathcal{O}(\lambda/L^2)$ with L the linear size of the finite lattice or the DCA cluster and λ a coefficient.[17] The faster convergence of the DCA corresponds to its smaller λ compared to finite size lattices.

In Fig. 7, the values of the $G(k=(0,\pi),\tau=\beta/2)$ and $G(k=(0,\pi),\tau=\beta/4)$ in Fig. 6 have been plotted versus $1/L^2$ for both the DCA and finite size results. The Green function behaves linearly as a function of $1/L^2$ for large L. The extrapolations of the DCA and finite size results meet as $L\to\infty$, approximating the value of the dressed Green function in the thermodynamic limit. The complementarity of DCA and finite size methods allows a determination of the thermodynamic limit of imaginary time Green functions with unprecedented accuracy.

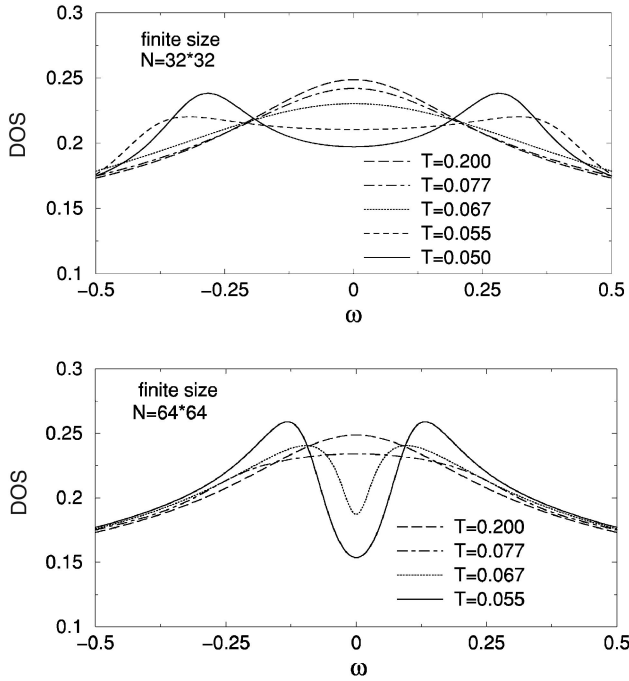As seen in Fig. 8, by increasing the size of a finite lattice,

FIG. 8. The FLEX density of states (DOS) for a 32×32 finite size lattice with periodic boundary conditions (top) vs energy for $U/t=1.57$ at various temperatures, and for a 64×64 finite size lattice (bottom). The evolution of a week pseudogap is observed at $T=0.067$ for the 64×64 lattice higher than $T=0.055$ for the 32×32 one and the pseudogap is also much broader for the 32×32 lattice [128×128 finite size lattice results were obtained by Deisz *et al.* (Ref. 9)].

the pseudogap occurs at higher temperatures and also becomes less pronounced (sharper) as we approach the actual size of an infinite real lattice. The DCA yields a complementary behavior, as shown in Fig. 9. By increasing the coarse-graining cluster size, similar to the finite size lattices, the pseudogap is shifted toward higher temperatures. However, unlike the finite size lattices, for the DCA the precursor becomes more pronounced (broader) as the cluster increases in size because the size of the lattice remains constant and the correlations are limited to the cluster size. Thus, comparatively, *the DCA underestimates the gap while the finite size calculation overestimates it.*

By comparing the results in Figs. 8 and 9 one may see that the 32×32 DCA cluster yields more realistic physics than the corresponding 32×32 finite size lattice. The 64×64 finite size lattice results are also close to those for the 32×32 DCA cluster at slightly lower T (e.g., $T=0.055$ for the finite size and $T=0.033$ for the DCA). However, since the sizes of clusters are considerably smaller than the sizes of lattices, the DCA significantly reduces the complexity of the problem and consequently the CPU time. In terms of the CPU time, the FLEX with the numerical Fourier transforms scales as $\mathcal{N}ln\mathcal{N}$ where $\mathcal{N}$ is the product of the total number of Matsubara frequencies and the k points in the first Brillouin zone. Hence, using a 32×32 cluster in place of a 64×64 lattice, both having 1024 Matsubara frequency points, roughly reduces the CPU time by a factor of 4.4. If the DCA
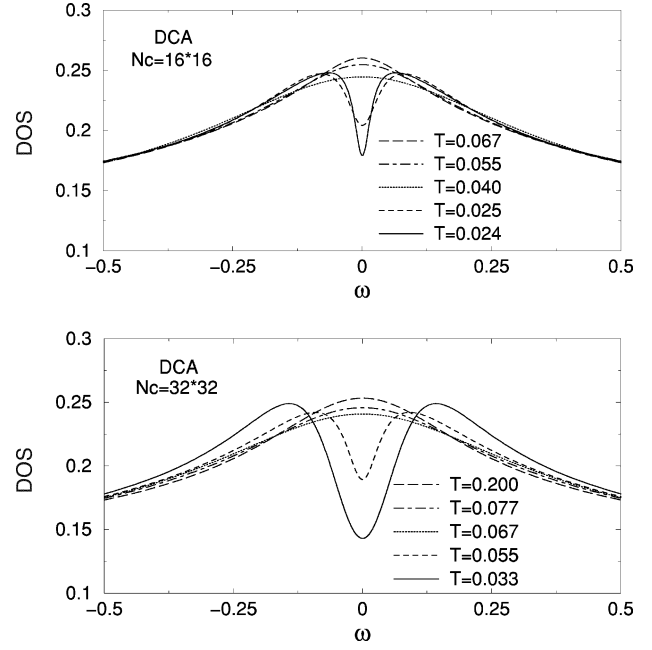

FIG. 9. The FLEX density of states (DOS) for a 16×16 DCA cluster (top) vs energy for $U/t=1.57$ at various temperatures, and for a 32×32 DCA cluster (bottom). For the 32×32 cluster, the evolution of a weak pseudogap is observed at $T=0.055$ higher than $T=0.025$ for the 16×16 one and the pseudogap is also broader for the 32×32 cluster.

cluster size N_c equals the size of the finite lattice N, the DCA requires somewhat more CPU time than the finite size lattice due to course-graining. Nevertheless, comparatively, for large finite lattices such as 64×64, the lattice size contributions to the CPU time significantly dominate the coarse graining ones in a 32×32 cluster. Thus, the 32×32 DCA cluster is much faster.

The FLEX often has difficulty reaching low temperatures. This is due to the fact that the χ_{ph} defined in Eq. (18) approaches unity as the temperature drops which in turn causes the $V^{(ph)}$ in Eq. (23) to diverge. In the DCA, χ_{ph} approaches unity more slowly, allowing the calculations to reach lower temperatures. One has to note that in the FLEX, the χ_{ph}^{DCA} is defined as

$$\chi_{ph}^{DCA}(\mathbf{Q},\omega_n)=-U(T/N_c)\sum_{\mathbf{K}}\sum_{m}\bar{G}(\mathbf{K}+\mathbf{Q},\omega_n+\omega_m)$$

$$\times\bar{G}(\mathbf{K},\omega_m), \tag{27}$$

with $\bar{G}$ defined in Eq. (5). Figure 10 illustrates the saturation of χ_{ph} for both the DCA and finite size lattices. The χ_{ph} for the 32×32 finite size lattice (filled circles) saturates at higher temperatures compared to the 32×32 DCA cluster (open diamonds), indicating that in the DCA, for a certain cluster size, the precursor to the phase transition can evolve to lower temperatures compared to a finite size lattice of the same size with periodic boundary conditions. However, for the correlation length $\xi>L$ the DCA approximation breaks down and
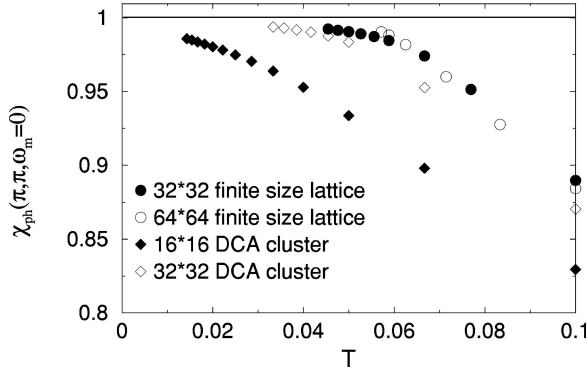
FIG. 10. The FLEX particle-hole bubble (χ_{ph}) at $Q=(\pi,\pi)$ and $\omega_m=0$ for a 16×16 and 32×32 DCA clusters (diamonds) and also for 32×32 and 64×64 finite size lattices with periodic boundary conditions (circles) vs temperature T at $U/t=1.57$. The relatively rapid saturation of the finite size lattice χ_{ph} compared to the more gradual approach of the DCA results towards unity is manifest [128×128 finite size lattice results were obtained by Deisz *et al.* (Ref. 9)].

replacing the self-energy by its coarse grained counterpart is no longer accurate. Here the DCA takes on a significant mean-field character.

Another feature of the Hubbard model near half-filling verified by the FLEX (Ref. 9) is a non-Fermi-liquid behavior. Here, this is studied by increasing the electron electron interaction U at a constant temperature. In Figs. 11 and 12 the real and imaginary parts of the self-energy at the X point (on the noninteracting Fermi surface) have been plotted versus energy for finite size lattices and the DCA respectively. As the interaction is increased, the negative slope in the real part turns positive around $\omega=0$ which is inconsistent with the requirement that the renormalization factor $[1-\partial\,\mathrm{Re}\,\Sigma(\mathbf{k}_F,\omega)/\partial\omega|_{\omega=0}]^{-1}$ should be smaller than unity in the Fermi-liquid theory. There also appears an anomalous inverted peak in the imaginary part at $\omega=0$.

As presented in Fig. 11, by increasing the length of the finite size lattice, the sharpness of the non-Fermi-liquid features is reduced. The same features for the DCA in Fig. 12 are slightly less pronounced, and, in a complementary fashion to the finite size lattices, their sharpness is enhanced by increasing the size of the cluster. Thus, again, the DCA underestimates the non-Fermi-liquid features while the finite size calculation overestimates it.

Earlier in Fig. 10 it was shown that the FLEX particle-hole bubble $\chi_{ph}(q,\omega_m=0)$ at $q=Q=(\pi,\pi)$ approaches unity as the temperature is lowered. This causes the spin-fluctuation T matrix

$$T_{\sigma,\sigma}(q,\omega_m)=\frac{3}{2}\left[\frac{\chi_{ph}(q,\omega_m)^2}{1-\chi_{ph}(q,\omega_m)}\right], \qquad (28)$$

which is just the third term in $V^{(ph)}(q,\omega_m)$ in Eq. (23) to peak around the $(Q,\omega_m=0)$ point. For real frequencies, $T_{\sigma,\sigma}(Q,\omega)$ has a sharp peak around $\omega=0$. Since $T_{\sigma,\sigma}(Q,\omega)$ is only used to construct the irreducible self-energy, within the DCA it is constructed from coarse grained Green func-
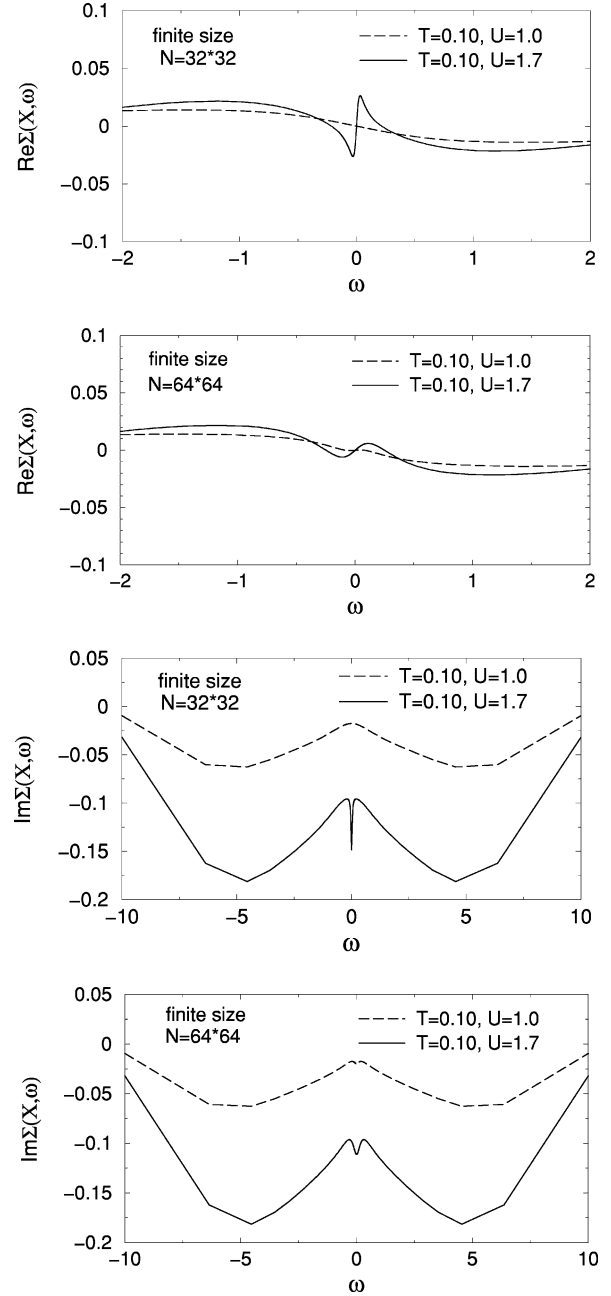

FIG. 11. The FLEX real (top two) and imaginary (bottom two) parts of the self-energy at the X point for 32×32 and 64×64 finite size lattices with periodic boundary conditions vs energy for $T=0.10$ and two different interactions U. The inverted peak at $\omega=0$ in the imaginary part and the positive slope in the real part are both signatures of non-Fermi-liquid behavior. For smaller lattice sizes these signatures are more pronounced [128×128 finite size lattice results were obtained by Deisz *et al.* (Ref. 9)].

tions. Thus the DCA counterpart of Eq. (28) is obtained by only replacing χ_{ph} with χ_{ph}^{DCA} defined in Eq. (27). Figures 13 and 14 show how this peak sharpens as the temperature decreases or interaction increases for finite size lattices and the DCA respectively. In the 64×64 finite size lattice (cf. Fig. 13, bottom), the peak continues to develop as the temperature is lowered and the interaction is raised. At $T=0.067$ and
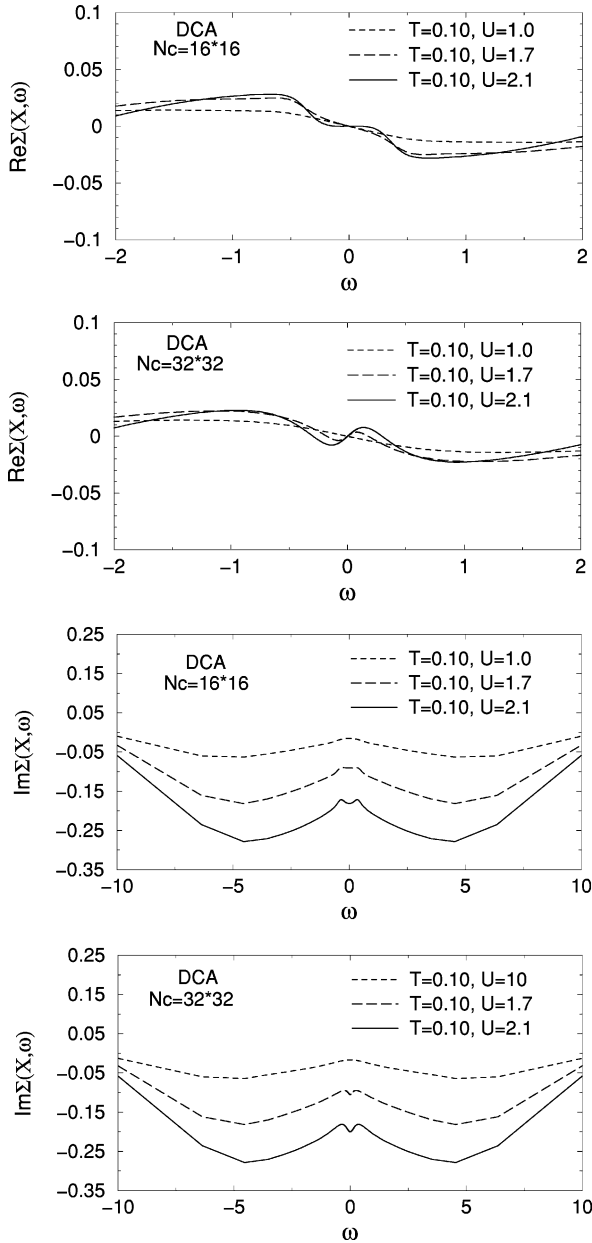
FIG. 12. The FLEX real (top two) and imaginary (bottom two) parts of the self-energy at the X point for 16×16 and 32×32 DCA clusters vs energy for $T = 0.10$ and two different interactions U. The non-Fermi-liquid features occur at slightly higher interactions compared to the finite size lattices. Upon increasing the cluster size, these features become more pronounced (complementary to the finite size lattices with periodic boundary conditions).

$U = 1.6$ where there exists a pseudogap in the DOS, the peak undergoes a significant growth compared to the other graphs shown in the same figure. The 32×32 (cf. Fig. 13, top) lattice presents the same behavior with a slightly sharper but shorter peak.

The DCA also illustrates the same type of peaks at a slightly higher interaction and lower temperatures for the 16×16 cluster (cf. Fig. 14, top). Increasing the cluster size to 32×32 gives rise to higher peaks similar to the finite size lattices case but unlike the finite size lattices peaks become sharper as the size is increased.

All the results illustrated in this section indicate the complementarity of the DCA to the finite size lattice scheme. It is also observed that the DCA is capable of reproducing relatively the same physics as the finite size FLEX at slightly different parameters but a lower CPU cost. The combination of these two facts makes this technique a good candidate to be employed in the numerical treatment of a wide range of many-body problems.

Lastly, to better understand the effect of the DCA cluster embedded in a fermionic bath, we can rewrite the course grained Green function defined in Eq. (5) as

$$\bar{G}(\mathbf{K}, z) = \frac{1}{z - \bar{\epsilon}_{\mathbf{K}} - \Sigma(\mathbf{K}, z) - \Gamma(\mathbf{K}, z)}. \qquad (29)$$

where $\bar{\epsilon}_K = N_c / N \sum_{\widetilde{\mathbf{k}}} \epsilon_{\mathbf{K} + \widetilde{\mathbf{k}}}$ and $\Gamma(\mathbf{K}, z)$ is the host function. Maier et al.,[6] defined

$$t_{\mathbf{K} + \widetilde{\mathbf{k}}} = \epsilon_{\mathbf{K} + \widetilde{\mathbf{k}}} - \bar{\epsilon}_{\mathbf{K}}, \qquad (30)$$

whereby $\Gamma(\mathbf{K}, z)$ can be expressed as

$$\Gamma(\mathbf{K}, z) = \frac{\dfrac{N_c}{N} \sum_{\widetilde{\mathbf{k}}} t^2_{\mathbf{K} + \widetilde{\mathbf{k}}} G(\mathbf{K} + \widetilde{\mathbf{k}}, z)}{1 + \dfrac{N_c}{N} \sum_{\widetilde{\mathbf{k}}} t_{\mathbf{K} + \widetilde{\mathbf{k}}} G(\mathbf{K} + \widetilde{\mathbf{k}}, z)}. \qquad (31)$$

By Taylor expanding $t_{\mathbf{K} + \widetilde{\mathbf{k}}}$ around the cluster points $\mathbf{K}$ it is found that $t_{\mathbf{K} + \widetilde{\mathbf{k}}} \sim \mathcal{O}(\Delta k)$ with $\Delta k = 2\pi / L$. Thus Eq. (31) yields $\Gamma(\mathbf{K}) \sim \mathcal{O}[(\Delta k)^2]$ as $\Delta k \to 0$. To illustrate this, we calculate $\Gamma(r = 0, \tau = 0)$ by summing over all the $\mathbf{K}$ points and ω_n frequencies, and plot it versus $(\Delta k)^2$. Figure 15 illustrates this linear behavior for $N_c \geq 16$. $N_c = 1$ holds complete mean field characters and no nonlocal fluctuations. $N_c = 4$ is anomalous, as explained in a paper by Betts et al.[15] There, the finite size cubic lattices with less than six (four in two-dimensional square lattices) distinct nearest neighbors per each site are not used in finite size scalings for estimating the physical properties of models like the spin one half XY ferromagnet or the Heisenberg antiferromagnet. For $N_c = 4$, because of the periodicity of the clusters, each cluster point is surrounded by two identical nearest neighbors in every direction and therefore has only two distinct nearest neighbors (cf. Fig. 16). Thus the effect of fluctuations are overestimated.[21] For $N_c > 4$ there is no such anomaly and hence, all the points present the linear behavior proven above. Nevertheless, calculations with $N_c = 4$ do a reasonable job in capturing the qualitative effects of corrections to the DMFA.

VIII. MICROSCOPIC THEORY OF THE DCA

In Sec. IV we defined the thermodynamic potential functional difference $\Delta\Omega(T, \mu)$ in terms of the Green function, self-energy, and $\Phi[G]$ [cf. Eq. (25)]. In Eq. (13), $\Phi[G]$ includes all the compact (skeletal) Feynman diagrams and the rest incorporates the entire noncompact contribution.[22] Typical compact and noncompact diagrams are illustrated in Fig. 17. The noncompact diagram (a) consists of two self-
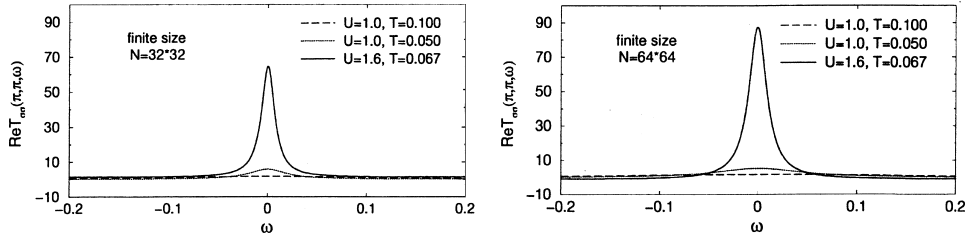
FIG. 13. The FLEX real part of the T matrix at $Q=(\pi,\pi)$ vs energy for 32×32 (top) and 64×64 (bottom) finite size lattices with periodic boundary conditions. For the 32×32 finite size lattice at $T=0.067$ and $U/t=1.6$ (solid), we observe a huge peak due to the formation of a pseudogap in the DOS. By increasing the lattice size to 64×64 a higher and broader peak occurs at the same temperature.

energy pieces σ and σ' connected with two one-particle Green functions. Removing these two Green functions would split the diagram into two separate pieces. In the compact diagram (b) two vertex parts Γ and Γ' with four Green functions are connected together. One can not split this type of diagrams into two separate pieces by just removing two one-particle Green functions. As mentioned earlier, in the DCA, we employ coarse grained Green functions to construct only the compact diagrams. The Green functions in noncompact diagrams are calculated directly using Eq. (26) in which the self-energy $\Sigma_{DCA}(\mathbf{K},z)$ is coarse grained [the circles at the top and the bottom of the noncompact diagram in Fig. 17(a)].

Earlier, in a shorter paper concerning the Hubbard model in particular,[11] we showed both analytically and numerically that the error produced by coarse graining the noncompact diagrams is significantly larger than the error produced by coarse graining the compact ones. Here, we would like to give a more general argument in real space. We wish to emphasize two points in this approach. First, since the derivation of the DCA in this section relies only upon the exponential fall off of the Green function as a function of distance, it is far more intuitive than the momentum space argument in Ref. 11. Second, it ties the derivation of the DCA to the original derivation of the DMFA in the limit of infinite dimensions, where similar arguments are employed.[14]

The exponential falloff behavior occurs naturally in high dimensions. In the tight-binding Hamiltonian [cf. Eq. (8)], the factor t corresponds to the hopping of electrons among nearest neighboring sites. Thus, one could show that the real space Green function $G(r)$ (we drop the frequency label from this point on for simplicity) for r nearest neighbor hops is proportional to $G(r)\sim t^r$ as $t\to0$. On the other hand, Metzner *et al.* and Müller-Hartmann[14,13] have shown that, in

D dimensions, the factor t should be renormalized as $t/\sqrt{D}$ in order to have a finite density of states width as $D\to\infty$. As a result of this renormalization,

$$G(r)\sim t^r\sim(1/\sqrt{D})^r\sim D^{-r/2}=e^{-r/r_s}$$

$$r_s=\frac{2}{\ln D}, \tag{32}$$

meaning that $G(r)$ falls off exponentially as a function of r.

In the DCA, we attempt to minimize the error due to coarse graining the Green function (and potentials) in the Feynman diagrams. Consider the first nontrivial correction to the coarse grained noncompact diagrams generated by replacing the explicit coarse grained Green function lines by the noncoarse grained ones as illustrated in Fig. 18,

$$\delta^{(1)}[\Delta\Omega_{ncp}]\sim\frac{1}{N}\sum_{\mathbf{k}}\ \sigma(\mathbf{K})\sigma'(\mathbf{K})G(\mathbf{k})^2-\frac{1}{N_c}\sum_{\mathbf{K}}\ , \tag{33}$$

$$\sigma(\mathbf{K})\sigma'(\mathbf{K})\bar{G}(\mathbf{K})^2,$$

where $\mathbf{K}$ are the coarse graining cell momenta and $\mathbf{k}=\mathbf{K}+\tilde{\mathbf{k}}$ include all the momenta in the first Brillouin zone shown in Fig. 2. In this derivation we also presume that the self-energy is $\tilde{\mathbf{k}}$ independent and the entire $\tilde{\mathbf{k}}$ dependence is embedded in the Green functions.

By breaking up the sums over $\mathbf{k}$ in Eq. (33) into $\mathbf{K}$ and $\tilde{\mathbf{k}}$ sums and writing all the G in terms of their Fourier transforms at the same time we get
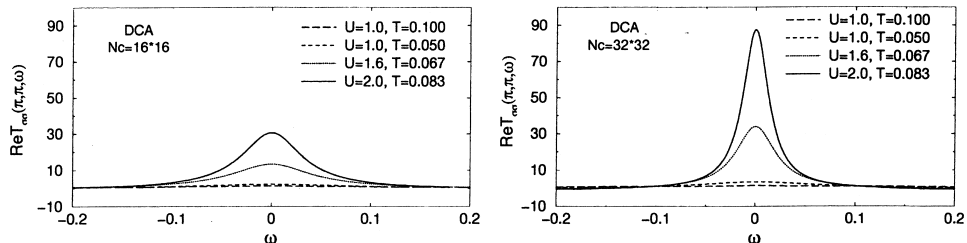

FIG. 14. The FLEX real part of the T matrix at $Q=(\pi,\pi)$ vs energy for 16×16 (top) and 32×32 (bottom) DCA clusters. Peaks similar to the finite size lattices appear at slightly higher interactions and lower temperatures. By increasing the cluster size, the peaks grow higher (similar to finite size lattices) and also sharpen (complementary to the finite size lattices).
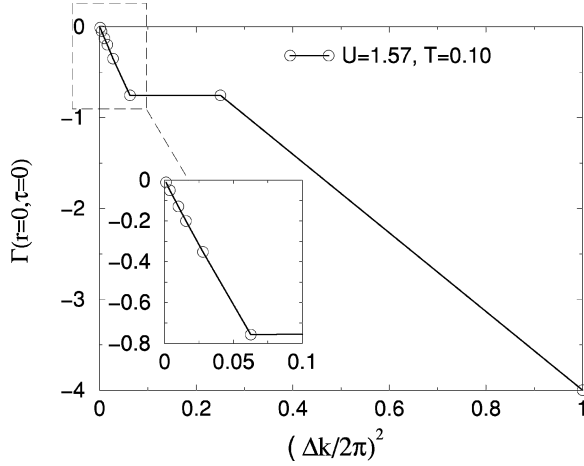
FIG. 15. The host function $\Gamma(r=0,\tau=0)$ vs $(\Delta k)^2$. The linear behavior beyond $N_c=4$ is manifest, also see the inset.

$$
\delta^{(1)}[\Delta\Omega_{ncp}] \sim \frac{1}{N} \sum_{\mathbf{k},\mathbf{K}} \sigma(\mathbf{K})\sigma'(\mathbf{K}) \sum_{\mathbf{x}_1,\mathbf{x}_2} G(\mathbf{x}_1)G(\mathbf{x}_2)
$$

$$
\times e^{-i\tilde{\mathbf{k}}\cdot(\mathbf{x}_1+\mathbf{x}_2)} e^{-i\mathbf{K}\cdot(\mathbf{x}_1+\mathbf{x}_2)} - \frac{N_c}{N^2}
$$

$$
\times \sum_{\mathbf{K},\tilde{\mathbf{k}}_1,\tilde{\mathbf{k}}_2} \sigma(\mathbf{K})\sigma'(\mathbf{K}) \sum_{\mathbf{x}_1,\mathbf{x}_2} G(\mathbf{x}_1)G(\mathbf{x}_2)
$$

$$
\times e^{-i\tilde{\mathbf{k}}_1\cdot\mathbf{x}_1} e^{-i\tilde{\mathbf{k}}_2\cdot\mathbf{x}_2} e^{-i\mathbf{K}\cdot(\mathbf{x}_1+\mathbf{x}_2)}, \tag{34}
$$

in which we used Eq. (5) for $\bar{G}(\mathbf{K})$. According to Fig. 2, we can split $\mathbf{x}=\mathbf{X}+\tilde{\mathbf{x}}$, where $\tilde{\mathbf{x}}$ extend between two separate clusters while $\mathbf{X}$ always remain within a single cluster. By making this separation in Eq. (34) one picks up phases including products of $-i\mathbf{K}\cdot\mathbf{X}$, $-i\mathbf{K}\cdot\tilde{\mathbf{x}}$, $-i\tilde{\mathbf{k}}\cdot\mathbf{X}$ and $-i\tilde{\mathbf{k}}\cdot\tilde{\mathbf{x}}$ in their exponents. The phase associated with the product $\mathbf{K}\cdot\tilde{\mathbf{x}} = 2n\pi$ with n an integer equals unity. The phases involving $-i\tilde{\mathbf{k}}\cdot\mathbf{X}$ products are also neglected as discussed in Sec. II. Hence, Eq. (34) can be rewritten as follows:
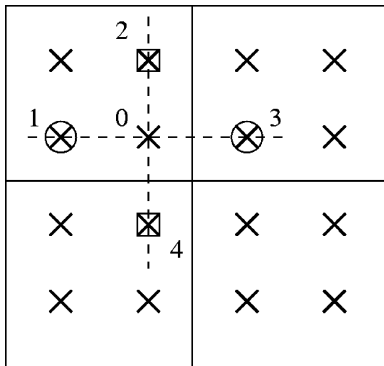

FIG. 16. DCA clusters in the real space lattice with $N_c=4$. Due to the periodicity of the clusters, points 2 and 4 in squares and 1 and 3 in circles are equivalent and therefore point 0 observes its nearest neighbors twice in each direction.
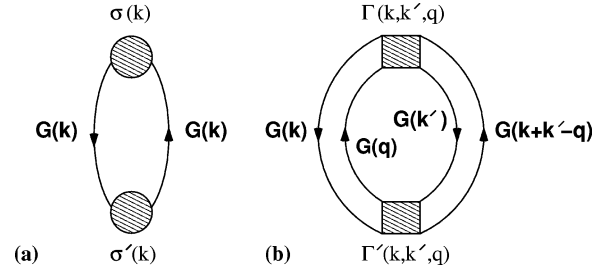

FIG. 17. (a) Typical noncompact (nonskeletal) and (b) typical compact (skeletal) diagrams.

$$
\delta^{(1)}[\Delta\Omega_{ncp}] \sim \frac{1}{N} \sum_{\mathbf{K}} \sigma(\mathbf{K})\sigma'(\mathbf{K}) \sum_{\mathbf{X}_1,\mathbf{X}_2} \sum_{\tilde{\mathbf{x}}_1,\tilde{\mathbf{x}}_2}
$$

$$
\times G(\mathbf{X}_1+\tilde{\mathbf{x}}_1)G(\mathbf{X}_2+\tilde{\mathbf{x}}_2)
$$

$$
\times e^{-i\mathbf{K}\cdot(\mathbf{X}_1+\mathbf{X}_2)} \sum_{\tilde{\mathbf{k}}} e^{-i\tilde{\mathbf{k}}\cdot(\tilde{\mathbf{x}}_1+\tilde{\mathbf{x}}_2)}
$$

$$
- \frac{N_c}{N^2} \sum_{\mathbf{K}} \sigma(\mathbf{K})\sigma'(\mathbf{K}) \sum_{\mathbf{X}_1,\mathbf{X}_2} \sum_{\tilde{\mathbf{x}}_1,\tilde{\mathbf{x}}_2}
$$

$$
\times G(\mathbf{X}_1+\tilde{\mathbf{x}}_1)G(\mathbf{X}_2+\tilde{\mathbf{x}}_2)
$$

$$
\times e^{-i\mathbf{K}\cdot(\mathbf{X}_1+\mathbf{X}_2)} \sum_{\tilde{\mathbf{k}}_1,\tilde{\mathbf{k}}_2} e^{-i\tilde{\mathbf{k}}_1\cdot\mathbf{x}_1} e^{-i\tilde{\mathbf{k}}_2\cdot\mathbf{x}_2}. \tag{35}
$$

Implementing the substitutions

$$
\sum_{\tilde{\mathbf{k}}} e^{-i\tilde{\mathbf{k}}\cdot(\tilde{\mathbf{x}}_1+\tilde{\mathbf{x}}_2)} = \frac{N}{N_c}\delta_{\tilde{\mathbf{x}}_1,-\tilde{\mathbf{x}}_2}
$$

and

$$
\sum_{\tilde{\mathbf{k}}_1,\tilde{\mathbf{k}}_2} e^{-i\tilde{\mathbf{k}}_1\cdot\mathbf{x}_1} e^{-i\tilde{\mathbf{k}}_2\cdot\mathbf{x}_2} = \left(\frac{N}{N_c}\right)^2 \delta_{\tilde{\mathbf{x}}_1,0}\delta_{\tilde{\mathbf{x}}_2,0}, \tag{36}
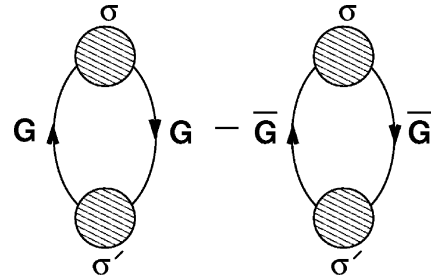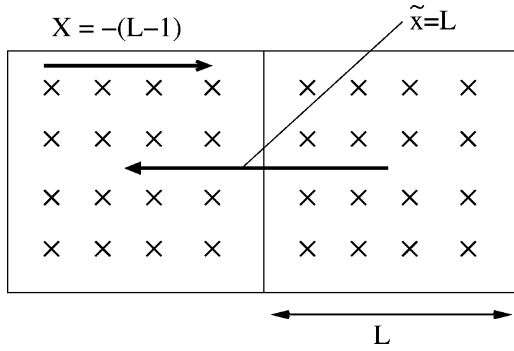$$

Eq. (35) simplifies into

FIG. 18. First correction by noncompact diagrams, $\delta^{(1)}[\Delta\Omega_{ncp}]$.

FIG. 19. Two adjacent clusters with their $\mathbf{X}$ and $\tilde{\mathbf{x}}$ vectors.

FIG. 20. First correction by compact diagrams, $\delta^{(1)}[\Delta\Omega_{cp}]$.

which indicates the existence of nonlocal corrections to the noncompact contribution of the thermodynamic potential even at infinite dimensions.

Now we replace the coarse grained self-energy bubbles in Fig. 18 with coarse grained vertices having four external legs, and look at the difference between compact diagrams with and without coarse grained Green functions which are explicitly shown in the figure. Since we earlier dropped the frequency labels in the Green functions, here we use indices 1, 2, 3, and 4 to emphasize that these Green functions have different frequency labels. The first correction to the compact contribution of the thermodynamic potential depicted in Fig. 20 is

$$\delta^{(1)}[\Delta\Omega_{ncp}] \sim \frac{1}{N_c} \sum_{\mathbf{K}} \sigma(\mathbf{K})\sigma'(\mathbf{K}) \Bigg[\sum_{\mathbf{X}_1,\mathbf{X}_2,\tilde{\mathbf{x}}} G(\mathbf{X}_1+\tilde{\mathbf{x}})$$

$$\times \mathbf{G}(\mathbf{X}_2-\tilde{\mathbf{x}})e^{-i\mathbf{K}\cdot(\mathbf{X}_1+\mathbf{X}_2)}$$

$$-\sum_{\mathbf{X}_1,\mathbf{X}_2} G(\mathbf{X}_1)G(\mathbf{X}_2)e^{-i\mathbf{K}\cdot(\mathbf{X}_1+\mathbf{X}_2)} \Bigg]. \quad (37)$$

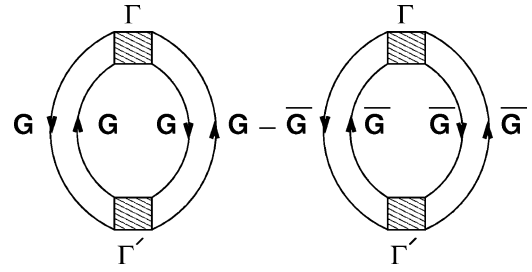Setting $\sigma(\mathbf{K})\sigma'(\mathbf{K}) = \xi(\mathbf{K})$ and performing the $\mathbf{K}$ summation,

$$\delta^{(1)}[\Delta\Omega_{ncp}] \sim \sum_{\mathbf{X}_1,\mathbf{X}_2} \xi(\mathbf{X}_1+\mathbf{X}_2) \Bigg[\sum_{\tilde{\mathbf{x}}} G(\mathbf{X}_1+\tilde{\mathbf{x}})\mathbf{G}(\mathbf{X}_2-\tilde{\mathbf{x}})$$

$$-G(\mathbf{X}_1)G(\mathbf{X}_2) \Bigg]$$

$$= \sum_{\mathbf{X}_1,\mathbf{X}_2} \xi(\mathbf{X}_1+\mathbf{X}_2) \sum_{\tilde{\mathbf{x}}\neq 0} G(\mathbf{X}_1+\tilde{\mathbf{x}})\mathbf{G}(\mathbf{X}_2-\tilde{\mathbf{x}}).$$

$$(38)$$

Knowing that $\xi(\mathbf{X}_1+\mathbf{X}_2) = \Sigma_\mathbf{X} \sigma(\mathbf{X})\sigma'(\mathbf{X}+\mathbf{X}_1+\mathbf{X}_2)$ and also that the lowest order of $\sigma(\mathbf{X}) \sim G^3(\mathbf{X}) \sim e^{-3|\mathbf{X}|/r_s}$ we conclude that in Eq. (38), the largest contribution is due to terms having $\mathbf{X}_1 = -\mathbf{X}_2$ or in other words, local ξ. As shown in Fig. 19, the first term in the $\tilde{\mathbf{x}}$ sum corresponds to $|\tilde{\mathbf{x}}| = L$ (size of the cluster) and $\mathbf{X}$ can be as large as $\mathbf{X} = -(L-1)$ in the opposite direction. Hence the leading order term in Eq. (38) falls off as

$$\delta^{(1)}[\Delta\Omega_{ncp}] \sim \xi(0)\times 2D\times G[L-(L-1)]G[-L+(L-1)]$$

$$\sim 2D\xi(0)e^{-1/r_s}e^{-1/r_s} = 2D\xi(0)e^{-2/r_s}, \quad (39)$$

where $2D$ is the number of $|\tilde{\mathbf{x}}| = L$ contributions in D different dimensions of a D-dimensional cubic lattice. In Eq. (39) we also used the fact that due to the lattice symmetry, $G(-\mathbf{X}) = G(\mathbf{X})$. As $D\to\infty$, using $r_s = 2/\ln D$,

$$\delta^{(1)}[\Delta\Omega_{ncp}] \sim 2D\xi(0)e^{-\ln D} = 2\xi(0)DD^{-1} \sim \mathcal{O}(1). \quad (40)$$

$$\delta^{(1)}[\Delta\Omega_{cp}] \sim \frac{1}{N^3} \sum_{\substack{\mathbf{k}_1,\mathbf{k}_2 \\ \mathbf{q}}} \Gamma(\mathbf{K}_1,\mathbf{K}_2,\mathbf{Q})\Gamma'(\mathbf{K}_1,\mathbf{K}_2,\mathbf{Q})$$

$$\times G_1(\mathbf{k}_1)G_2(\mathbf{k}_2)G_3(\mathbf{q})G_4(\mathbf{k}_1+\mathbf{k}_2-\mathbf{q})$$

$$-\frac{1}{N_c^3} \sum_{\substack{\mathbf{K}_1,\mathbf{K}_2 \\ \mathbf{Q}}} \Gamma(\mathbf{K}_1,\mathbf{K}_2,\mathbf{Q})\Gamma'(\mathbf{K}_1,\mathbf{K}_2,\mathbf{Q})$$

$$\times \bar{G}_1(\mathbf{K}_1)\bar{G}_2(\mathbf{K}_2)\bar{G}_3(\mathbf{Q})\bar{G}_4(\mathbf{K}_1+\mathbf{K}_2-\mathbf{Q}),$$

$$(41)$$

where, similar to Eq. (33), all the vertices are coarse grained but the Green functions are not. Following the same procedure as for the noncompact difference, we arrive at

$$\delta^{(1)}[\Delta\Omega_{cp}] \sim \sum_{\substack{\mathbf{X}_1,\mathbf{X}_2 \\ \mathbf{X}_3,\mathbf{X}_4}} \Lambda(\mathbf{X}_1+\mathbf{X}_4,\mathbf{X}_2+\mathbf{X}_4,\mathbf{X}_3-\mathbf{X}_4)$$

$$\times \Bigg[\sum_{\tilde{\mathbf{x}}} G_1(\mathbf{X}_1-\tilde{\mathbf{x}})G_2(\mathbf{X}_2-\tilde{\mathbf{x}})$$

$$\times G_3(\mathbf{X}_3+\tilde{\mathbf{x}})G_4(\mathbf{X}_4+\tilde{\mathbf{x}})$$

$$-G_1(\mathbf{X}_1)G_2(\mathbf{X}_2)G_3(\mathbf{X}_3)G_4(\mathbf{X}_4) \Bigg], \quad (42)$$

where

$$\Lambda(\mathbf{X}_1+\mathbf{X}_4,\mathbf{X}_2+\mathbf{X}_4,\mathbf{X}_3-\mathbf{X}_4)$$

$$=\frac{1}{N_c^3}\sum_{\substack{\mathbf{K}_1,\mathbf{K}_2\\\mathbf{Q}}}\Gamma(\mathbf{K}_1,\mathbf{K}_2,\mathbf{Q})\Gamma'(\mathbf{K}_1,\mathbf{K}_2,\mathbf{Q})$$

$$\times e^{-i\mathbf{K}_1\cdot(\mathbf{X}_1+\mathbf{X}_4)}e^{-i\mathbf{K}_2\cdot(\mathbf{X}_2+\mathbf{X}_4)}e^{-i\mathbf{Q}\cdot(\mathbf{X}_3-\mathbf{X}_4)}$$

$$=\sum_{\substack{\mathbf{X},\mathbf{X}'\\\mathbf{X}''}}\Gamma(\mathbf{X},\mathbf{X}',\mathbf{X}'')\Gamma'(\mathbf{X}+\mathbf{X}_1+\mathbf{X}_4,\mathbf{X}'+\mathbf{X}_2+\mathbf{X}_4,\mathbf{X}''$$

$$+\mathbf{X}_3-\mathbf{X}_4). \tag{43}$$

Once again, the largest contribution is associated with local Λ, i.e., $\mathbf{X}_1=-\mathbf{X}_4$, $\mathbf{X}_2=-\mathbf{X}_4$ and $\mathbf{X}_3=\mathbf{X}_4$. Therefore,

$$\delta^{(1)}[\Delta\Omega_{cp}]\sim\sum_{\mathbf{X}}\Lambda(0)\left[\sum_{\widetilde{\mathbf{x}}}G_1(-\mathbf{X}-\widetilde{\mathbf{x}})G_2(-\mathbf{X}-\widetilde{\mathbf{x}})G_3(\mathbf{X}\right.$$

$$+\widetilde{\mathbf{x}})G_4(\mathbf{X}+\widetilde{\mathbf{x}})-G_1(\mathbf{X})G_2(\mathbf{X})G_3(\mathbf{X})G_4(\mathbf{X})\Big]$$

$$=\Lambda(0)\sum_{\mathbf{X},\widetilde{\mathbf{x}}\neq 0}G_1(\mathbf{X}+\widetilde{\mathbf{x}})G_2(\mathbf{X}+\widetilde{\mathbf{x}})$$

$$\times G_3(\mathbf{X}+\widetilde{\mathbf{x}})G_4(\mathbf{X}+\widetilde{\mathbf{x}}). \tag{44}$$

Considering $|\widetilde{\mathbf{x}}|=L$ and $\mathbf{X}_{min}=-(L-1)$,

$$\delta^{(1)}[\Delta\Omega_{cp}]\sim\Lambda(0)\times 2D\times G_1[-L+(L-1)]G_2[-L+(L$$

$$-1)]G_3[L-(L-1)]G_4[L-(L-1)]$$

$$=2D\Lambda(0)e^{-4/r_s}=2\Lambda(0)D^{-1},\quad\left(r_s=\frac{2}{\ln D}\right),$$

$$\tag{45}$$

which vanishes as $D\rightarrow\infty$.

Comparing Eq. (45) with Eq. (40) shows that the first correction to the compact contribution of the thermodynamic potential falls off exponentially twice as fast as the equivalent correction in the noncompact contribution. In addition, even at the infinite dimensional limit, there are corrections of order 1 to the noncompact contribution, whereas for the compact diagrams the DCA becomes exact and there are no corrections. This justifies coarse graining only in the compact diagrams. The Green functions in the noncompact diagrams have to be explicitly constructed from the coarse-grained self-energy $\Sigma_{DCA}(\mathbf{K},\omega_n)$ using Eq. (26).

In Fig. 21, the compact contribution of the thermodynamic potential difference constructed by coarse grained Green functions is plotted versus $(\Delta k)^2=1/L^2$. The variation of $\Delta\Omega_{cp}$ over the entire $1/L^2$ range is about 1%. At very low temperatures ($T<0.066$ in the inset), some deviation from linearity is observed due to the correlation length exceeding the cluster size L, and therefore the approximation of $\Sigma(k)$ by $\Sigma_{DCA}(K)$ begins to break down. Figure 22 illustrates the noncompact contribution sketched versus $1/L^2$ using both coarse grained and noncoarse grained Green functions. Using noncoarse grained Green functions, the variation of $\Delta\Omega_{ncp}$
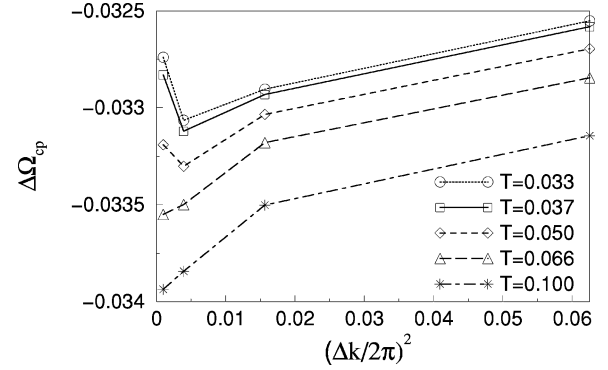

FIG. 21. The compact contribution to the thermodynamic potential vs $(\Delta k)^2$ at $U/t=1.57$ and various temperatures, using coarse-grained Green functions. The deviation from linearity at the lowest temperatures hint at the correlation length exceeding the cluster size.

over the entire $1/L^2$ range is roughly 30%. Coarse graining the Green functions in these diagrams can even change the sign of this noncompact contributions, clearly indicating that coarse graining the Green function is an unrealistic approximation for noncompact diagrams. However, one notices that for large cluster sizes the coarse grained and noncoarse grained results approach each other as the approximation to the infinite lattice becomes better.

IX. DCA IN FREQUENCY SPACE

As illustrated for the momentum space, the DCA results in a significant reduction of the problem complexity and it is complementary to the finite size lattice approach. In analogy to the momentum space, one could consider dividing the one-dimensional Matsubara frequency space into a number of coarse graining subcells. For both fermions and bosons, each cell should include an odd number of frequencies in order for the frequencies in the centers of these cells to preserve Fermionic or Bosonic properties. Figure 23 represents how the frequency space can be divided into coarse graining subcells each comprising a central Ω_n frequency and a num-
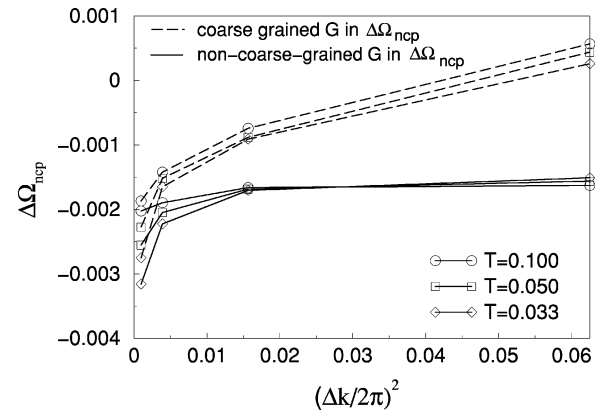

FIG. 22. Noncompact contribution to the thermodynamic potential vs $(\Delta k)^2$ at $U/t=1.57$ with and without coarse grained Green functions. Using coarse grained Green functions can result in a noncompact contribution with the wrong sign.
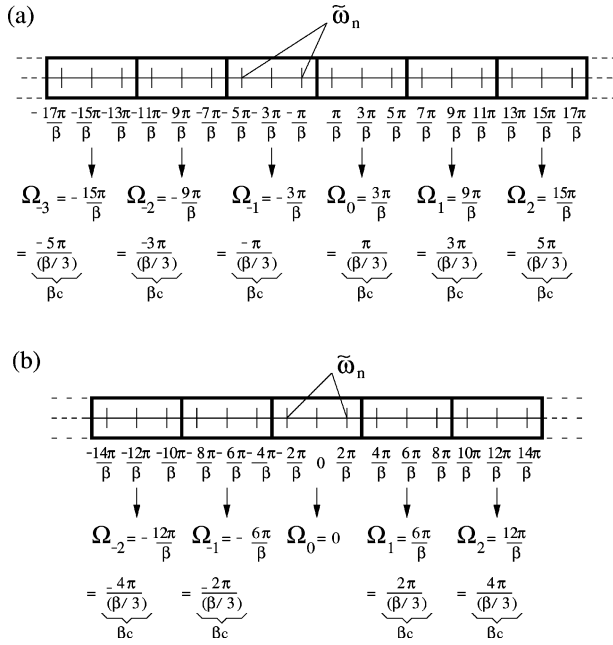
FIG. 23. Dividing the fermion (a) and boson (b) Matsubara frequency spaces into subcells. The central Ω_n frequencies can be written in the form of the original lattice with renormalized β denoted as β_c ($\beta_c = \beta/3$ in this case).

ber of coarse graining $\tilde{\omega}_n$ lying around it. The central Ω_n frequencies can be rewritten in the form of the original lattice with renormalized β shown as β_c in the figure. Similar to the case of the momentum space, we make the following transformation for the Laue function:

$$\Delta = \beta \; \delta_{\omega_{n1},\omega_{n2}+\omega_{n3}} \rightarrow \Delta_{DCA} = \beta_c \; \delta_{\Omega_{n1},\Omega_{n2}+\Omega_{n3}}. \quad (46)$$

For the Matsubara frequencies of the vertex shown in Fig. 1 considering frequency dependent interactions in general (in condensed matter physics, most of the interactions are indeed simultaneous and thus frequency independent). As a result, we may again coarse grain the Green function over the subcell frequencies

$$\bar{G}(\mathbf{K},\Omega_n) = \frac{\beta_c}{\beta} \sum_{\tilde{\omega}_n} G(\mathbf{K},\Omega_n + \tilde{\omega}_n). \quad (47)$$

According to Fig. 24, the full coarse graining of the Green function amounts to $\beta_c \rightarrow 0$ which causes all the self-energy Feynman diagrams ordered higher than first (Hartree-Fock diagrams) to vanish and consequently we arrive at a fully static problem.

Unfortunately, we can show that coarse graining over Matsubara frequencies can lead to the violation of causality and as a result, the DCA is not systematically implementable for the Matsubara frequency quantities. The simplest example is the noninteracting Green function coarse grained as follows:[23]
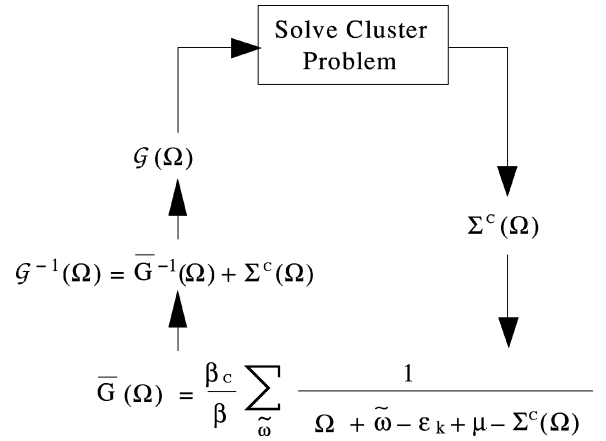

FIG. 24. The algorithm for the cluster solvers such as the NCA in which at each step before using the cluster solver the bare Green function is calculated by excluding the cluster self-energy. This is the only step through the algorithm where problems with causality might occur.

$$\bar{G}^{(0)}(\mathbf{K},\Omega_n) = \frac{\beta_c}{\beta} \sum_{\tilde{\omega}_n} G^{(0)}(\mathbf{K},\Omega_n + \tilde{\omega}_n)$$

$$= \frac{\beta_c}{\beta} \sum_{\tilde{\omega}_n} \frac{1}{i\Omega_n + i\tilde{\omega}_n - \epsilon_k + \mu}. \quad (48)$$

The retarded Green function is derived by the substitution $i\Omega_n \rightarrow \Omega + i\eta$:

$$\bar{G}^{(0)}_{ret}(\mathbf{K},\Omega) = \frac{\beta_c}{\beta} \sum_{\tilde{\omega}_n} \frac{1}{\Omega + i\eta + i\tilde{\omega}_n - \epsilon_k + \mu}. \quad (49)$$

The theory of analytic functions of a complex variable tells us that in order for the Green function to remain retarded in the time space, $\bar{G}^{(0)}_{ret}(\mathbf{K},\Omega)$ must not have any poles in the upper half plane of Ω. In Eq. (49), one could readily create poles in the upper half plane for negative $\tilde{\omega}_n$ which causes causality violation and consequently unphysical results.

The way around this difficulty is to use real frequencies even at finite temperatures. By invoking real frequencies we no longer coarse grain over imaginary values. Therefore, the retarded Green function will never acquire poles in the upper half plane and remains causal as shown below

$$\bar{G}_{ret}(\mathbf{K},\Omega) = \frac{N_{\tilde{\omega}}}{N_{\omega}} \sum_{\tilde{\omega}} \frac{1}{\Omega + \tilde{\omega} + i\eta + - \epsilon_k + \mu - \Sigma_{ret}(\mathbf{K},\Omega)}, \quad (50)$$

with N_{ω} the total number of frequencies and $N_{\tilde{\omega}}$ the number of those we coarse graining over in each cell. In an article by Hettler et al.,[4] a formal proof of causality is given (based on a geometrical argument) for coarse graining in the momentum space. This proof can be straightforwardly applied to the real frequency space as well and it extends the application of real frequency DCA not only to the perturbative cluster solvers such as the FLEX but also techniques like the NCA.

Lastly, similar to the momentum space, care must be taken when choosing the the size of the frequency coarse-graining cells. One must make sure that the cells are not larger than some characteristic energy scale (e.g. the Kondo temperature T_K) as the coarse graining would then suppress the relevant physics.

X. CONCLUSIONS AND OUTLOOK

We introduce and examine the DCA in detail by employing it with the FLEX to study the half filled two dimensional Hubbard model. The FLEX is not as precise as nearly exact techniques such as the quantum Monte Carlo approximation in describing the Hubbard model at strong interaction regime. However, it is capable of illustrating the utility of the DCA, including its complementarity and convergence compared to finite size lattice approaches. The DCA and finite size calculations (with periodic boundary conditions) both converge with corrections $\mathcal{O}(\lambda/L^2)$; however, in our example the coefficient λ_{DCA} was smaller than λ_{FS}, and of opposite sign indicating that the DCA converges more quickly and from a complementary direction. This complementarity was also seen in other quantities such as the pseudogap in the density of state and the non-Fermi liquid behavior that the DCA (finite size) calculation systematically under (over) estimates.

We also provide a detailed microscopic definition of the DCA by inspecting the error generated by coarse graining the Green functions in the compact and noncompact contributions to the thermodynamic potential. We conclude that due to the large magnitude of error that it generates, coarse graining the Green function in the noncompact part should be avoided and only the compact contribution should undergo coarse graining. It also appears that coarse graining the

Green functions over the Matsubara frequencies can and will lead to a violation of causality and therefore is pathological. Nevertheless, one can coarse grain the Green function over real frequencies and preserve the causality not only for the FLEX but also cluster solvers such as NCA in which the cluster contribution to the coarse grained dressed Green function is excluded before being inserted into the cluster solver.

The outlook for the FLEX-DCA approach is promising. Although the FLEX fails to accurately describe short-ranged physics such as moment formation (and related phenomena like the Mott gap), it does a good job describing long-ranged physics associated with spin and charge fluctuations. On the other hand, numerically exact calculations such as the QMC method are too expensive to perform for large clusters, and are thus restricted to the study of short-length scales. However, since the DCA gives us a way of parsing the problem into different length scales, it may be used to combine the short-length scale information from the QMC method with the long length scale information from the FLEX. This may be accomplished, by embedding a QMC cluster, of size L, into a much larger FLEX cluster of size $L' \gg L$, which is itself embedded in a mean field. As we have shown here, this approach should be implemented by approximating the generating functional $\Phi \approx \Phi_{QMC}(L) - \Phi_{FLEX}(L) + \Phi_{FLEX}(L')$. Work along these lines is in progress.

[1] T. Pruschke, M. Jarrell, and J. K. Freericks, Adv. Phys. **42**, 187 (1995).

[2] A. Georges, G. Kotliar, W. Krauth, and M. Rozenberg, Rev. Mod. Phys. **68**, 13 (1996).

[3] P. G. J. van Dongen, Phys. Rev. B **50**, 14016 (1994).

[4] M. H. Hettler, M. Mukherjee, M. Jarrell, and H. R. Krishnamurthy, Phys. Rev. B **61**, 12739 (2000).

[5] M. H. Hettler, A. N. Tahvildar-Zadeh, M. Jarrell, T. Pruschke, and H. R. Krishnamurthy, Phys. Rev. B **58**, 7475 (1998).

[6] Th. A. Maier, M. Jarrell, Th. Pruschke, and J. Keller, Eur. Phys. J. B **13**, 613 (2000).

[7] N. E. Bickers, D. J. Scalapino, and S. R. White, Phys. Rev. Lett. **62**, 961 (1989).

[8] N. E. Bickers and S. R. White, Phys. Rev. B **43**, 8044 (1990).

[9] J. J. Deisz, D. W. Hess, and J. W. Serene, Phys. Rev. Lett. **76**, 1312 (1996).

[10] J. W. Serene and D. W. Hess, Phys. Rev. B **44**, 3391 (1991).

[11] K. Aryanpour, M. H. Hettler, and M. Jarrell, Phys. Rev. B **65**, 153102 (2002).

[12] Y. Imai and N. Kawakami, cond-mat/0204093 (unpublished).

[13] E. Müller-Hartmann, Z. Phys. B: Condens. Matter **74**, 507 (1989).

[14] W. Metzner and D. Vollhardt, Phys. Rev. Lett. **62**, 324 (1989).

[15] D. D. Betts and G. E. Stewart, Can. J. Phys. **75**, 47 (1997).

[16] G. Baym, Phys. Rev. **127**, 1391 (1962).

[17] Th. A. Maier and M. Jarrell, Phys. Rev. B **65**, 041104(R) (2002).

[18] H. J. Vidberg and J. W. Serene, J. Low Temp. Phys. **19**, 179 (1977).

[19] J. J. Deisz, D. W. Hess, and J. W. Serene, cond-mat/9411026R [*Recent Progress In Many Body Theories*, edited by E. Schachinger *et al.* (Plenum, New York, in press), Vol. 4].

[20] M. A. Jenkins and J. F. Traub, Comm. ACM **15**, 97 (1972). The routine is available at http://www.netlib.org/tomspdf/419.pdf.

[21] Th. Maier (private communication).

[22] A. A. Abrikosov, L. P. Gorkov, and I. E. Dzyaloshinski, *Methods of Quantum Field Theory in Statistical Physics* (Dover, New York, 1975).

[23] T. Pruschke (private communication).